Supporting Materials
Deconvolution-Free Subcellular Imaging with Axially Swept Light-Sheet Microscopy

Kevin M. Dean, Philippe Roudot, Erik S. Welf, Gaudenz Danuser, and Reto Fiolka

Department of Cell Biology, University of Texas Southwestern Medical Center, 6000 Harry Hines Blvd., Dallas, Texas 75390, USA.

Microscope Setup

Two continuous wave lasers (488 nm, 500 mW, Coherent Sapphire, and 561 nm, 300 mW, MPB Communications) were independently shuttered with acousto-optic modulators (AOM-402AF1, IntraAction Corp.) and aligned into a common optical path with a dichroic mirror (LM01-466-25, Semrock). The 488 and 561 nm lasers were focused through a 30-micron pinhole and expanded to beam diameters of 12 and 10.8 mm ($1/e^2$), respectively. In order to provide uniform illumination intensity at the sample, the beam was truncated with an iris, allowing only the central portion of the beam to be used for imaging. A half-wave plate provided control of the beam polarization. A cylindrical lens (f = 50 mm, LJ1695RM-A, ThorLabs) focused the beam to a line profile that was relayed to the image plane of the remote focusing arm of the microscope with an achromatic doublet (f = 80 mm, ThorLabs), a Z-galvo mirror (6210HSM40B, Cambridge Technologies), a telecentric f-theta lens (f = 60 mm, S4LFT0061/065, Sill Optics), an infinity-corrected tube lens (ITL200, ThorLabs), and a 40x 0.8 NA water-dipping objective (Nikon Instruments). A quarter-wave plate and polarizing beam splitter were placed intermediate to the back pupil plane of the remote focusing objective and the tube lens.

A 7 mm mirror mounted to a flexure-guided piezo actuator (P-603.3S2, Physik Instrumente) was placed at the focal plane of the remote focusing objective. This piezo actuator has a nominal unloaded resonance frequency of 410 Hz and a closed loop range of 300 microns. The line focus was reflected off of the mirror and recollected by the same objective. Because the light passed through the quarter-wave plate a second time, the polarization of the reflected light was rotated by 90 degrees, and was consequently reflected by the polarizing beam splitter. Light transmission through and reflection off of the polarizing beam splitter was optimized with rotation of the half-wave and quarter-wave plates, respectively. The back pupil plane of the remote focusing objective was imaged 1:1 to the back pupil plane of the excitation objective with two infinity-corrected tube lenses (ITL200, ThorLabs). While it is possible to use an air objective for the remote focus, we note that in most cases this will require some degree of magnification between the two pupil planes. This in turn limits the choice of high-quality lenses that are available to construct a telescope that maintains telecentric scanning of the beam. In contrast, with an 1:1 imaging ratio, it is straight forward to build such a telescope with two identical scan or tube lenses. Telecentric scanning of the laser beam is mandatory to keep the light-sheet parallel to the imaging plane throughout the entire Z-range. The use of high quality optics to relay laser light from the scan mirror and the remote focusing objective to the illumination objective is necessary to minimize chromatic aberrations. If present, focal shifts in the Y-direction for different illumination wavelengths can be addressed by synchronizing each pixel readout of each camera to its illumination wavelength individually. However, wavelength dependent shifts in the Z-direction when acquiring a 3D stack need to be minimized optically. With our implementation and scan range we did not experience such issues, but we refrained from using simple achromatic doublets to relay the objectives and the scan mirror.

The microscope can be operated in high- and low-NA modes. In the high-NA mode (NA = 0.8), the back pupil of the objective was overfilled. In the low-NA mode (NA = 0.29), a variable-width slit was translated into the beam path in a location conjugate to the back pupil plane of the objective (*e.g.*, immediately adjacent to the Z-galvo). This resulted in a truncated beam that underfilled the back pupil of the objective and decreased the effective illumination NA. The width of the line was measured directly in the pupil plane of the objective and allowed us to calculate the effective illumination NA.

A third 40x 0.8 NA water-dipping objective (Nikon Instruments), aligned orthogonal to the excitation objective, served as the detection objective. The detection objective was scanned synchronously with the illumination beam position with a piezo stage (Nano F-450, Mad City Labs). Fluorescence leaving the detection objective was spectrally separated and isolated for multicolor imaging with an ultra-flat dichroic mirror (T565lpxr, Chroma) and band pass emission filters (ET525/50m and ET600/50m, Chroma), respectively, within the infinity space of the microscope. Subsequently, each fluorescence channel was individually imaged onto the active area of separate sCMOS cameras (Flash 4.0 v2, Hamamatsu) with infinity-corrected tube lenses (ITL200, ThorLabs). Because of the synchronous readout of the active pixels in the light-sheet operation of the camera, an additional mirror was necessary to obtain an even number of reflections in the reflected (green fluorescence) optical path. With an odd number of reflections, the two cameras would be mirror images along the X-direction to each other and consequently, the image of the laser line would move in opposite directions.

To generate 3D data, a single image was acquired at each plane by sweeping the axial position of the beam once and integrating one frame on the sCMOS camera in “light-sheet mode”. Once completed, the Z-galvo mirror and detection objective were moved to a new focal plane, and another image was acquired. The step size in the Z-direction was adjusted to 160 nm and 450 nm in the high- and low-NA modes, respectively. The distance necessary to traverse two Rayleigh lengths of the beam was used to determine the number of active pixels. In the high-NA mode, with a Rayleigh length of 0.617 microns, 8 pixels were used (1.28 microns). In the low-NA mode, with a Rayleigh length of 4.88 microns, 60 pixels were used (9.6 microns). For time lapse imaging, the laser power delivered to the sample was varied between ~360 nW and 18 μW. For characterization of instrument performance (optical sectioning, resolution, etc.), laser powers of 1-124 μW were routinely used. Imaging of the collagen matrix, as a result of the poor brightness of the DyLight fluorophore, required 390 μW of laser power. All laser powers reported were measured at the back pupil plane of the excitation objective.

For optimal image quality and signal strength, the (i) illumination beam and camera must be synchronized, (ii) and the illumination beam must be located in the focal plane of the detection objective. To achieve this, it is useful to use a dense 3D distribution of fluorescent beads in a block of agarose or a fluorescently labeled collagen matrix. Because a level of labeling sparseness is required, fluorescent solutions are not recommended. To align the microscope, we position the remote focusing mirror in the middle of its trajectory, and align the central waist of the line focus to the middle of the sCMOS camera. The correct focal plane for the detection objective is identified when the in-focus strip of light is most narrow. The scan of the line focus (with a matching scan range for the camera FOV previously calibrated) and the light-sheet mode on the sCMOS camera are then activated. The synchronization of the line focus and the active pixels is apparent when the fluorescence signal peaks and only in-focus objects are detected. The synchronization can be optimized by either adjusting an electronic delay between the onset of the piezo mirror scanning and the camera readout or by slightly translating the camera with a micrometer stage. Since the camera is demagnified into the sample plane, a reasonably fine adjustment can be performed with a standard translation stage. When focusing deeper into a collagen sample, slight spherical aberrations will shift the apparent position of the line focus as well as the focal plane of the objective relative to the light-sheet plane. Hence to obtain the best imaging performance, the focal plane of the detection objective and the synchronization of the line focus to the camera readout need to be readjusted for each imaging location. We typically only need to change these parameter in the order of one micrometer per 100 micron depth. For the acquisition of large z-stacks, we implemented a dynamic correction for the scan synchronization to account for this, which can be modified by the user.

Instrument Control and Data Acquisition

Instrument control and data acquisition was executed with custom LabView (National Instruments) software written and maintained by Coleman Technologies that is under license from Howard Hughes Medical Institute, Janelia Farm Research Campus. All synchronization commands were delivered to the microscope with a field-programmable gate array (PCIe-67852R, National Instruments) running on an 8-core Windows 8 machine equipped with RAID-0 configured solid-state drives, RAID-0 configured 7200 RPM hard-drives, and 96 Gb of RAM. The two cameras were operated in the “light-sheet mode” and were precisely triggered with the start of the sawtooth waveform that was driving the remote-objective mirror. A 10% 'fly-back' time was applied to the sawtooth waveform.

Mammalian Cell Culture and Labeling

MV3 melanoma cells were cultured in Dulbecco’s modified eagle medium (DMEM) supplemented with 10% fetal bovine serum and 10 units/mL pen/strep, and were a gift from Dr. Peter Friedl (MD Anderson Cancer Center). MV3 cells were infected with lentivirus encoding cytosolic mNeonGreen or Tractin-EGFP under a constitutive cytomegalovirus promoter (1). Human retinal pigment epithelial (RPE-1) cells immortalized with human telomerase reverse transcriptase (hTERT) were purchased from ATCC and cultured in DMEM F12 supplemented with 10% fetal bovine serum, 10 units/mL pen/strep and 0.01 mg/mL hygromycin B. These cells were genome-modified with TALEN technology to express mEmerald-vimentin and TagRFP-T-β-Tubulin (2) from their native genomic loci, and characterization of these cells will be published elsewhere. Single particle tracking was performed on ARPE cells (spontaneously immortalized retinal pigment epithelial cells, a gift from Dr. Jerry Shay, University of Texas Southwestern Medical Center) ectopically expressing clathrin-light chain fused to EGFP under a cytomegalovirus promoter. ARPE cells were maintained in antibiotic-free DMEM F12 supplemented with 10% fetal bovine serum. The collagen matrix was labeled with an affinity-based protein, CNA35 (3, 4), that had been expressed in *E. coli*, purified, and fluorescently tagged using N-hydroxysuccinimide-ester chemistry (DyLight 521, ThermoScientific). For optical sectioning measurements, cells were treated with ~50 μM blebbistatin to decrease blebbing.

Sample Preparation

Samples for initial experiments were performed as previously reported (5). Briefly, fresh solutions of 1% ultra-pure agarose in deionized water were prepared, briefly subjected to negative pressure to remove excess dissolved air, and placed into a custom Teflon mold that mounted the agarose to a dovetail upon polymerization. A small volume of the agarose was excluded with a square stainless steel pin with flat interfaces positioned towards the excitation and detection objectives. Once molded, the stainless steel plug was removed and the agarose was incubated in Ca^{2+}, Mg^{2+} free phosphate-buffered saline (PBS). Collagen was prepared from chilled reagents to prevent premature polymerization of the matrix, and included 50 μL of 10x-concentrate PBS, 250 μL collagen (4.88 mg/mL rat tail collagen type I, Corning, or bovine collagen I), 200 μL of deionized water, and sodium hydroxide to neutral pH. Cells were removed from the culture flasks with trypsin, neutralized, and excess media was aspirated from the cell pellet following centrifugation. Immediately afterwards, the cell pellet was resuspended carefully in the chilled collagen mixture, placed in the agarose mold, and allowed to polymerize at 37 degrees.

In an effort to minimize the effect of building vibrations on microscope performance, subsequent experiments were performed within a 1 mm thick 3D collagen matrix adsorbed to a 5 mm diameter coverslip. Imaging was performed on the solvent-exposed side of the collagen matrix with a 45-degree excitation and detection optical interface. In both cases, cells were imaged 2-48 hours after placement in the collagen. Imaging was performed at 37 degrees Celsius in phenol-free DMEM supplemented with 10% fetal bovine serum, 10 units/mL pen/strep, 2 mM GlutaMax, and 25 mM HEPES.

Image Analysis and Single Particle Tracking

EGFP-tagged clathrin light chains (EGFP-CLC) have been tracked in an automated fashion using Matlab (Mathworks) tools previously published in our lab (6, 7). Here, EGFP-CLC puncta detection is performed using a three-dimensional implementation of the algorithm described by Aguet *et al.* (7). For each time point, a filtering step first estimates the probable loci of diffraction-limited spots. On a voxel-by-voxel basis, this filter estimates the amplitude, background, and variance of a three-dimensional Gaussian as defined by the PSF of the optical system. This information is used to estimate the likelihood of a diffraction-limited object being present using a double-sided t-test. P-values < 0.05 are considered positive for object detection. This filter allows for fast, locally adaptive, and very sensitive thresholding for possible events.

For each local maximum on the Laplacian-of-Gaussian filtered volume that coincides with the mask of significance, a Gaussian model is fitted to estimate the amplitude, scale, background and position at a sub-resolved level. This estimation is carried out by solving a non-linear least square problem with a Levenberg–Marquardt optimization scheme. The goodness-of-fit test is performed again to test for other spurious detections after the first sub-pixel-resolved approximation. In order to fully automate the detection process, the scale used in the filtering steps is estimated offline. This pre-processing step applies the detection algorithm with a scale of 1.5 voxel, the first mode of the distribution of estimated scale is used to calibrate the algorithm. The u-track algorithm (6) was used to link the detected EGFP-CLC particles into consistent tracks. CLC puncta diffusion is modeled through conventional Brownian motion. The proposed parameterization is a classic setup for diffusing object tracking. The parameter minTrackLen is set to 5 time-points (~40 sec) to avoid visual clutter and ensure consistency of tracks.

Optical Simulations

Optical simulations were performed with Matlab (MathWorks) on either a normal desktop PC or a Linux server running 168 CPU nodes and 384 Gb of RAM. Intensity profiles for Bessel and Lattice beams were computed two-dimensionally in the ZX plane and in the corresponding Fourier plane. Bessel beams were simulated by modeling their Fourier transform as a thin annulus of finite thickness. The lattice modes were computed by multiplying such an annulus by a corresponding comb function to yield the necessary beam spacing in real space. The data was then transformed into real space by a two dimensional fast Fourier transform (FFT). The intensity distribution was computed by taking the squared modulus at each pixel for 1-photon modes and the modulus to the power of four for the 2-photon modes. The annulus width for the desired beam propagation length was computed by Equation 1, which was derived from the focusing properties of a laser beam and simple geometric considerations:

$$FWHM_Y = \frac{8 \cdot \lambda \cdot \eta}{\pi \cdot (NA_{OD} - NA_{ID}) \cdot (NA_{OD} + NA_{ID}) \cdot 1.699} \quad (1)$$

Where λ is the vacuum wavelength of light, NA_{ID} and NA_{OD} are the inner and outer NA of the annulus, respectively, η is the refractive index of the immersion media (1.333 for water) and 1.699 is an empirical factor to obtain the FWHM. Using this formula, we were able to very closely reproduce the values reported by *Gao et al*. (8). The laser line focus was simulated in 2D in the ZY plane by forward-propagating a wavefront that has passed through an ideal lens. Thus it was assumed that the beam would not change in the X-direction. The intensity distribution of the laser line focus was again computed by taking the squared modulus at every pixel. To compute the time averaged illumination profile of the light-sheet, the focus was convolved with a line of one pixel width that was running along the propagation direction (Y). To compute the effective illumination profile in ASLM, the laser line focus was truncated around its beam waist to a length of two Rayleigh lengths. The truncation was performed with a top-hat filter that was blurred at its edges with the simulated detection PSF. The truncated line focus was convolved with the same line of pixels running in the Y direction as it was done with the time-averaged illumination profile.

Comparison with 2-Photon Laser Scanning Confocal Microscopy

Cells embedded within polymerized collagen were imaged with an upright Zeiss LSM780 equipped with a 1.8 mm working distance 20x W Plan-Apochromat NA 1.0 water-dipping objective and non-descanned GaAsP detectors for fluorescence detection. A Chameleon (Coherent) laser emitting at 900 nm was used for 2-photon excitation. The voxel size was set to 160 x 160 x 160 nm, and Z-stacks were collected with the motorized nosepiece. Frame averaging was performed to increase the SNR of the data.

Comparison with 2-Photon Bessel beam LSFM

A 2-photon Bessel beam microscope as presented by Planchon *et al*. (9) was constructed with the main difference that the propagation distance of the Bessel beam was increased to a FWHM of ~100 microns by using a thinner annulus. Two Nikon 40x NA 0.8 objectives were used for illumination and fluorescence detection. The microscope was operated in the digital scanned light-sheet mode, i.e., the Bessel beam performed a continuous sweep through the sample plane to synthesize a light-sheet. The cells were mounted in a 1 mm thick 3D collagen matrix adsorbed to a 5 mm diameter coverslip, and imaged at 45 degrees relative to the detection objective. This is analogous to the geometry used by Planchon *et al*. (9).

Supporting Notes

Note S1. Increase in Out-of-Focus Blur with Propagation length.

To quantify the out-of-focus illumination that results from light sheets generated by ASLM, dithered lattice (hexagonal and square), or laterally swept Bessel beams, we performed numerical simulations (9, 10). Each beam was simulated for a 15-, 30-, 50-, 75-, and 150-micron propagation length (FWHM). Throughout the simulations, the maximum NA was 0.64, and accordingly, the minimum NA of the annulus was varied to change the beam propagation length for the lattice and Bessel beams. The excitation wavelength for 1- and 2-photon was 488 and 900 nm, respectively. For clarity, Figure S1 shows the results only for a subset of the simulations (15-, 50-, and 150- microns beam lengths). As the propagation length increased, each mode suffered from increased side lobe energy density. This was particularly evident for 1-photon Bessel illumination (Figure S1A), where at a 150-micron propagation length the side lobes spanned ±150-microns (±10-microns shown) from the main lobe of the beam. In contrast, the 2-photon Bessel illumination (Figure S1B) maintained a narrow illumination profile up to the maximum propagation length simulated here (150-microns). The 1-photon square lattice maintained excellent illumination confinement within its central lobe for all propagation lengths tested. However, the width of the central lobe increased drastically with the illumination propagation length. For example, the 15-, 50-, and 150-micron propagation lengths had central lobe FWHM of 0.863, 1.61, and 4.24 microns, respectively. Commonly, in propagation invariant beams, the central lobe FWHM does not change with propagation length (e.g. Figure S1A and B), suggesting that the 1-photon square lattice is significantly Gaussian in character. In contrast, the 1-photon hexagonal lattice maintained a narrow central lobe FWHM, but was increasingly accompanied by strong resonances as the propagation length increased (Figure S1D). The high- and low-NA time averaged light-sheets in ASLM (Figure S1E and F) follow a similarly shaped beam skirt as 1-photon Bessel beam LSFM. The red dashed line in Figure 1E and F illustrates the effective illumination profile that the active pixels in ASLM detect. It remains invariant over the range of propagation lengths shown here and enables ASLM to image large field of views without accumulating overwhelming blur on the detector.

To more quantitatively describe the effect these light sheet profiles have on imaging, we defined the in-focus signal as that originating from within the detection depth-of-focus (~1.1 microns). All excitation energy located outside of the depth-of-focus contributes to image blur that obscures the in-focus signal. For simplicity, nodes in the detection point spread function were not considered and it is assumed that widefield detection captures all out-of-focus light. We also assumed a large and homogeneously labeled sample which gives rise to fluorescence proportional to the local excitation intensity. Figure S2 shows the percent in-focus signal for each imaging mode as a function of beam propagation length. For ASLM, we included simulation results for a scenario where all pixels on the camera would be active simultaneously ("nondescanned") and when an active pixel strip of a width of 2 Rayleigh lengths descans the fluorescence signal ("descanned", which is the normal operation mode of ASLM). While we do not operate ASLM in a "nondescanned" mode in practice, the corresponding curves are of interest, as they represent the out-of-focus excitation load that is imposed on the sample. While the majority of the out-of-focus fluorescence light is not detected in ASLM, its excitation still occurs and may lead to bleaching of the fluorophores.

1-Photon Bessel beam microscopy shows the worst percentage of in-focus signal over the range of propagations lengths. For example, at a propagation length of 150-microns, the 1-photon Bessel beam signal consists of up to 95% blur. 2-photon Bessel beam illumination maintains a much higher percentage of in-focus signal. Nevertheless, even with 2-photon illumination, the finite energy density located in the side lobes diminished the in-focus signal at large propagation lengths (Inset, Figure S1B, and Figure S2). The high- and low-NA ‘nondescanned’ modes of ASLM are very similar to hexagonal and square lattice, respectively. This means that these microscope techniques impose a similar amount of out-of-focus excitation on a sample. Importantly, ASLM maintains the same Z-resolution for all propagation lengths simulated, whereas the Z-resolution in square lattice decreases with increasing propagation length (Figure S1C).

Another important difference to the other techniques is obvious when one compares the descanned modes of ASLM (the way ASLM is operated in practice), which measure how much in-focus information is effectively detected. The high-NA ASLM mode maintains an excellent percentage of in-focus signal over the full range of propagation lengths. The in-focus information in the low-NA mode first decreases slightly over small propagation lengths but then settles at around 85%. The drop can be explained that for the short propagation lengths, the light sheet is not yet fully averaged and the intensity profiles as well as the in-focus percentage was computed from the center position of the resulting light sheet. At large propagation lengths, it becomes obvious that ASLM faces massively reduced amounts of out-of-focus blur in its image raw data compared to the other techniques. Of the other techniques, only 2-Photon Bessel beam LSFM can provide a reasonable confinement of its excitation light and fluorescence detection.

Numerical deconvolution methods are routinely applied to the other LSFM methods that are compared here. But successful recovery of the in-focus signal has only been reported for short propagation lengths, *i.e.*, when the microscopes were operated with sufficient excitation confinement. The large amounts of blur that these techniques face at long propagation lengths may prove critical for deconvolution methods. For low photon counts, a situation may be reached where the shot noise contained in the out-of-focus blur exceeds the in-focus signal, making the numerical retrieval of the in-focus information problematic.

Note S2. The effect of imaging depth on signal strength and optical performance.

To measure the effects of light scattering and aberrations induced by the collagen matrix, we performed volumetric imaging with increasing imaging depth. We used a square shaped block of collagen that was polymerized in a cavity in a block of agarose. Light scattering and aberrations of the illumination light is assumed to mainly affect the Z-resolution (the thickness of the light-sheet mainly determines the resolving power in the Z-direction), whereas the lateral resolving power of the microscope is mainly affected by scattering and aberrations in the detection path. The overall attenuation of the fluorescence signal is dependent on both, excitation and emission path. We therefore increased both the illumination path as well as the detection path in collagen in equal steps of 250 and 500 microns. Surprisingly, the 3D optical resolving power was maintained at all imaging depths and therefore individual fibers are well resolved and can still be clearly distinguished even at 500 microns depth. This situation requires a homogeneously polymerized Matrix with no bubbles or distortions of its interfaces, which however can be achieved with careful sample preparation. The overall fluorescent signal, measured as the mean volumetric fiber intensity averaged over three realizations of this experiment, decayed notably at 250 and even more sharply at 500 microns depth. This suggests that the decay is mainly caused by light scattering removing ballistic light. However, while ballistic light is reduced, the scattering did not strongly affect the shape of the ballistic foci and hence good resolving power can be maintained in all directions. In other words, little aberrations appear to be introduced by the collagen matrix. We note that there is a slight refractive index mismatch between water and collagen. Therefore the alignment of the focal plane to the light-sheet and the synchronization of the line focus scan to the camera readout had to be slightly adapted to account for mild spherical aberration and a corresponding focal shift. We however conclude that the loss of signal by light scattering (accompanied by a loss of sectioning power due to more blur caused by scattered light) to be the limiting factor for imaging depth and not (spherical) aberrations.

Note S3. Quantification of the optical sectioning strength

To evaluate the optical sectioning capacity of our setup, we performed an automatic approach implemented in Matlab (MathWorks). Our method measures the intensity variation along the Z-axis in the volume surrounding the cell and adapted to the local curvature of the cell membrane. The only user input is the coarse estimation of the distance D along the Z-axis that defines the length of the area used to estimate the edge response. D is fixed to 7 microns in all experiments.

We used 3D imaging of collagen-embedded MV3 metastatic melanoma cell labeled with cytosolic mNeonGreen acquired with ASLM, 2-Photon laser scanning confocal microscopy and 2-photon Bessel beam LSFM. In order to provide an unbiased measurement of the cell edge response, only data sets that contained a single cell with a relatively spherical shape were selected.

The algorithm performs the following steps. A first approximation of the cell mask is obtained using an Otsu threshold. We then define a cylindrical mask in the Z-direction to target the optical sectioning, discarding the majority of the lateral contribution to the volume gradient. To do so, we erode the cell mask laterally using a cubic structural element of size $(D, D, 0)$ followed by a dilation in the Z-direction using a structural element of $(0,0,2D)$. In order to measure the intensity at distance $x \in [0, D]$ (resp. $[-D, 0]$) from the cell membrane, we isolate multiple one-voxel-wide bands using D dilations (resp. erosion) of the cell Mask with a cubic structural element of size (3,3,3) (see Figure 4 and Figure S5**)**. The algorithm automatically adjusts values for D that are too high for the cell size and/or the acquisition volume. The average intensity is computed in each band, yielding a sigmoidal profile along the Z-axis for each cell (see Figure 4E). In order to cope with the variability of the Otsu threshold outcome across each setups, the central band is reassigned to the one with an average intensity that is closest to the half of the sigmoid amplitude. For comparison purposes each sigmoid is then normalized from 0 to 1. The constant background value variation across setups can be offset but is negligible in our experiments. Cells were preliminarily treated with ~50 μm blebbistatin to reduce possible artifacts introduced by blebs. However, experiments on non-treated cells have shown similar results (data not shown).

The haze ratio is computed using the spatially average intensity measured beyond the estimated cell edge (defined by the center of the sigmoid) divided by the spatially averaged intensity measured inside the cell.

Supporting Figures

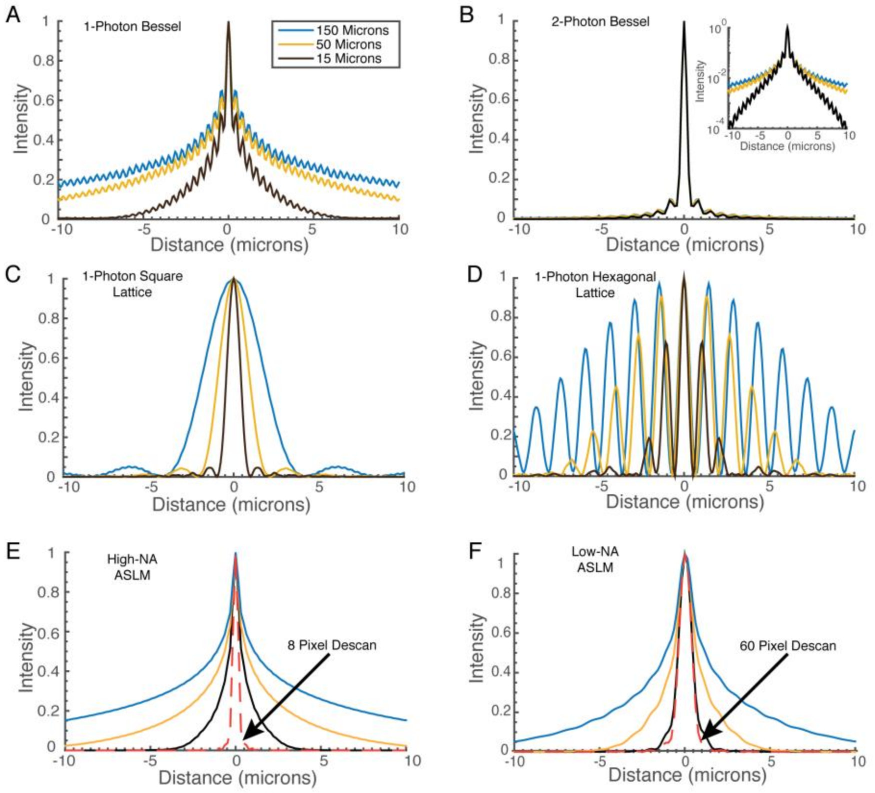

Figure S1. Comparison of the illumination profile in the Z-direction for time averaged light-sheets of varying propagation lengths (15, 50, and 150 microns, in Y-direction). For 2-photon excitation, the squared intensity values are plotted. (A) 1-photon Bessel beam LSFM, (B) 2-photon Bessel beam LSFM, (C) 1-photon square lattice LSFM and (D) 1-photon hexagonal lattice LSFM. (E) High-NA (0.64) and (F) low-NA (0.29) ASLM. The red curve, indicated by an arrow, shows the effective illumination profile as detected by the active pixels of the camera. To facilitate comparison with published data (8, 10), the maximum NA in the simulations was 0.64 for every microscope technique and the wavelength was 488 and 900 nm, for 1-photon and 2-photon excitation, respectively.

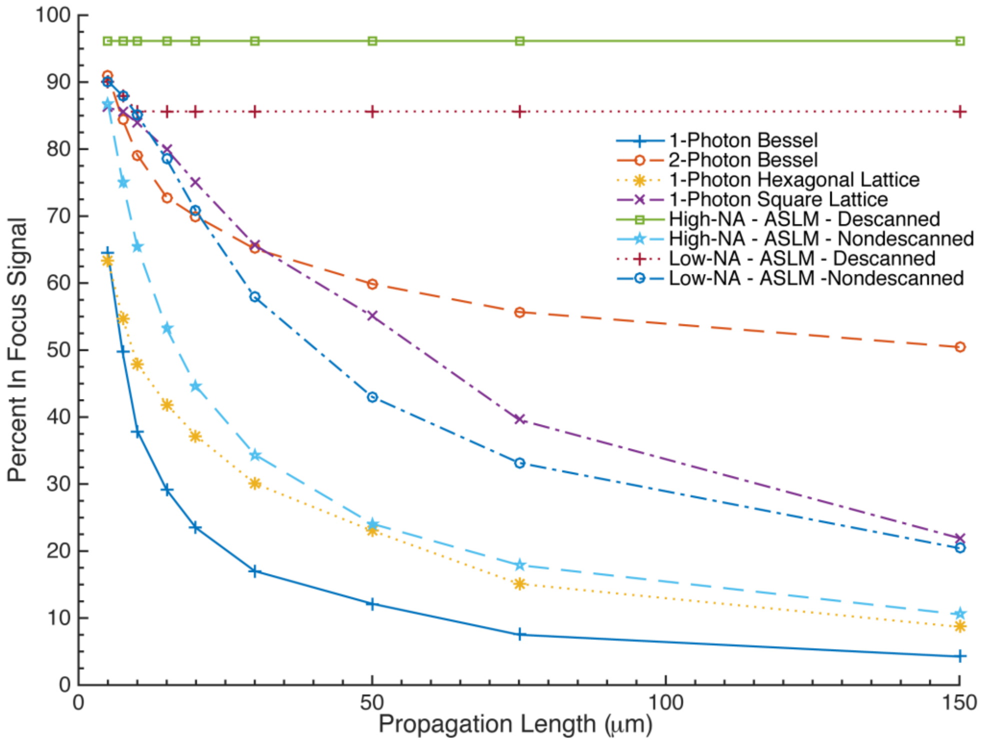

Figure S2. Percentage of in-focus signal (*i.e.*, excitation energy located within the 1.1 micron depth of focus) for different imaging modes. Squared intensity values are used for 2 Photon absorption. For ASLM, ‘descanned’ refers to data image acquisition in the 'light-sheet' mode, and thus only measures the effective illumination profile. In contrast, ‘nondescanned ‘is the total illumination that the sample experiences.

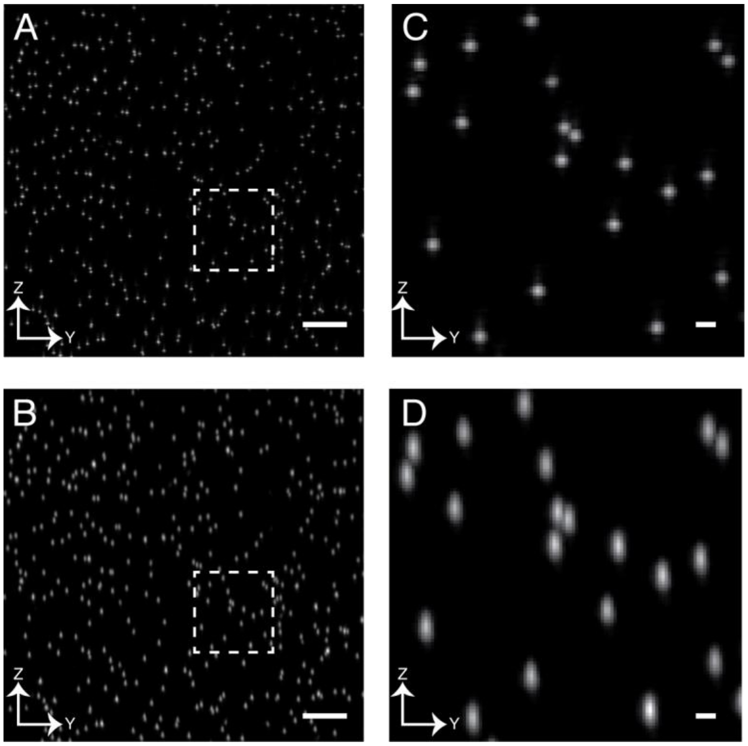

Figure S3. 200 nm fluorescent nanospheres embedded in agarose as imaged by ASLM. (A) YZ view (MIP over 16 microns in X) of a constellation of beads imaged in the ASLM with the high- and (B) low-NA modes, respectively. Panels C and D provide magnified views of the boxes in Panel A and B, respectively. Scalebar: A and B: 10 microns: (C) and (D): 1 micron.

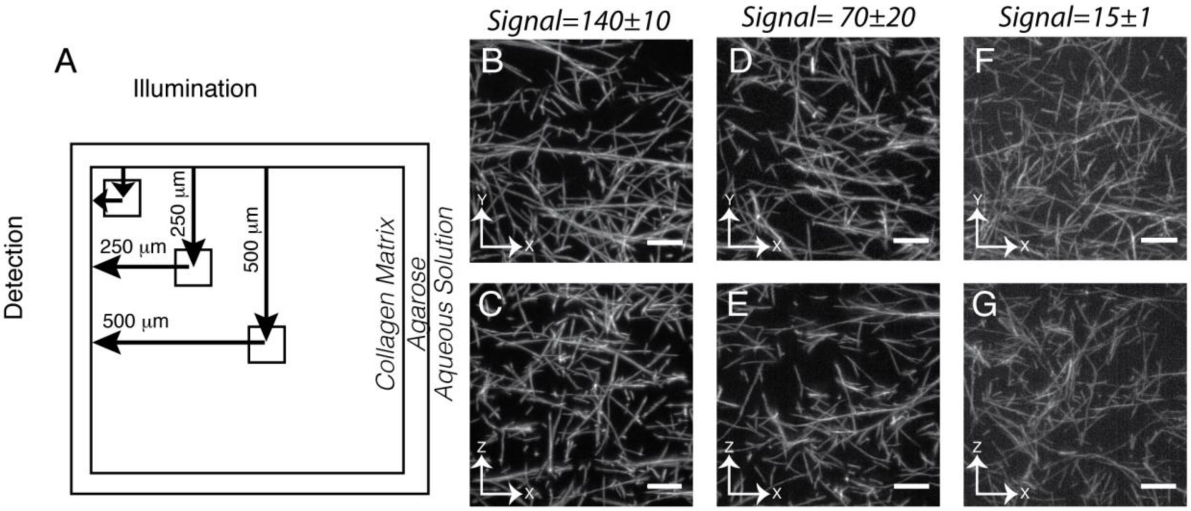
Signal=140±10
Signal= 70±20
Signal=15±1
A
Illumination
Detection
250 μm
500 μm
250 μm
500 μm
Collagen Matrix
Agarose
Aqueous Solution
B
C
D
E
F
G
Y
X
Z

Figure S4. Effects of scattering and aberrations when imaging at increasing depth into a cube of collagen. ‘Signal’ is the mean fiber intensity measured for three different volumes at each depth position and the standard deviation for these three measurements is reported as well. The sample was moved relative to the illumination and detection optics with a precision 3D stage. (A) Approximate center location of the imaging volumes measured from the collagen/agarose interface. (B) XY and (C) XZ view of collagen fibers imaged closest to the corner of the collagen cube. (D) XY and (E) XZ view of an imaging volume located 250 microns within the collagen cube. (F) XY and (G) XZ view of an imaging volume located 500 microns within the collagen cube. All views are maximum intensity projections over a depth of 4 microns. Scale bar: 10 microns.

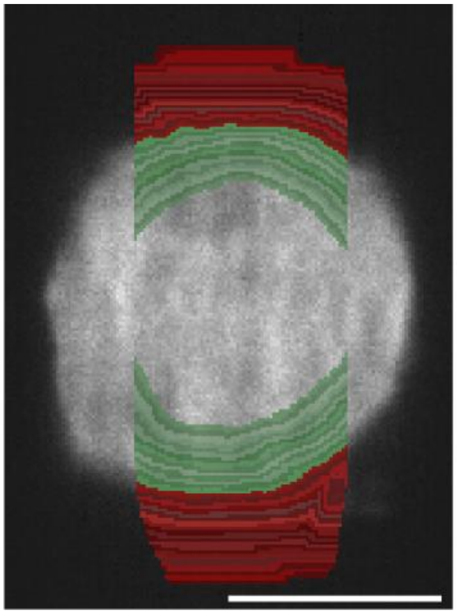

Figure S5. Localization of intensity measurements for optical sectioning strength evaluation. The example shows a slice of collagen-embedded MV3 metastatic melanoma cell labeled with cytosolic mNeonGreen imaged with ASLM. The colored mask represents the band where the intensity is measured. Shades of greens represent bands of intensity up to 5 microns inside the cell while the shade of red highlight the intensity measured up to 6 microns outside of the cell (scale bar 10 microns).

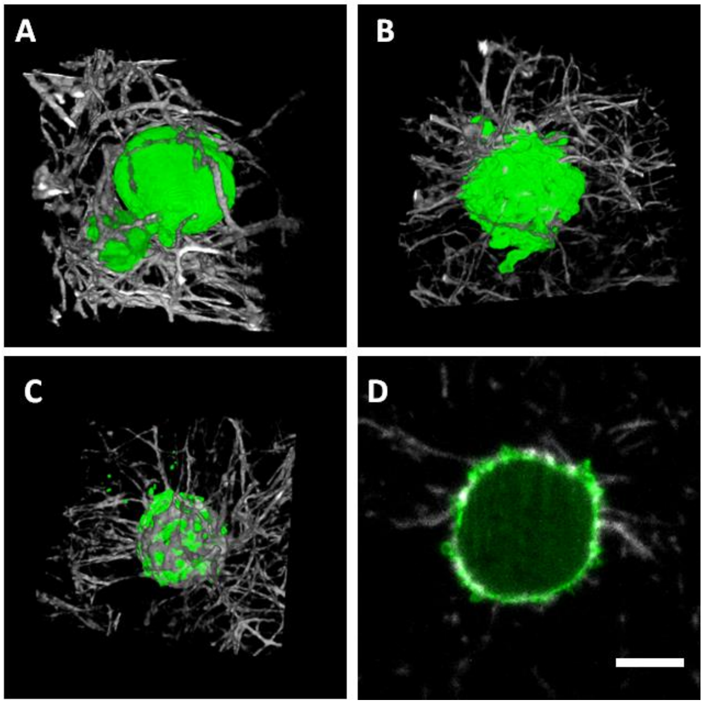

Figure S6. Enlarged 3D renderings of selected MV3 cells labeled with Tractin-EGFP from the imaging volume shown in Figure 3. (A) Cell showing a smooth cortex with no blebs. (B) A cell with many blebs and two large protrusions. (C) Cell actively reorganizing the collagen matrix. Panel A and B are 3D renderings of 45 x 45 x 45 micron volume. Panel C is a 3D rendering of a 45 x 45 x 15 micron volume. (D) Single XY section through the cell shown in panel C, highlighting the sequestration of collagen (grey) and enrichment of F-actin (green) in the cell cortex. Scale bar 10 microns.

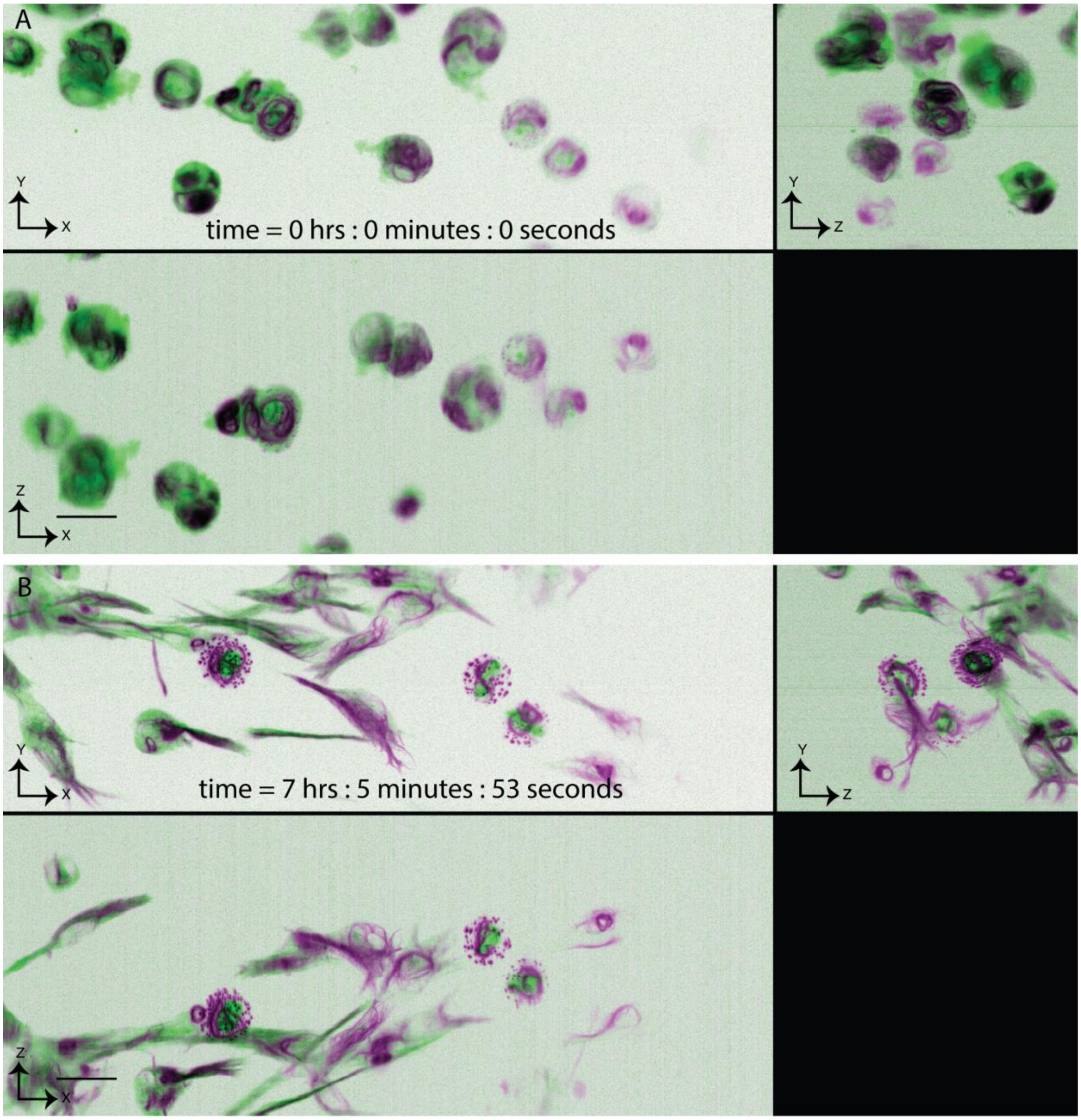
A
Y
X
time = 0 hrs : 0 minutes : 0 seconds
Y
Z
Z
X
B
Y
X
time = 7 hrs : 5 minutes : 53 seconds
Y
Z
Z
X

Figure S7. Maximum intensity projections along Z-, X-, and Y-dimensions of two selected time points from a volumetric time-lapse series of collagen-embedded RPE-1 cells labeled with mEmerald-vimentin (magenta) and TagRFP-microtubules (green). (A) 1st and (B) 86th time points. The whole series encompassed 120 time points (Movie S1). The color intensities are represented in a reciprocal scale to better highlight weak structures. Microtubules have a gamma correction of 0.8. Scale bar 20 microns.

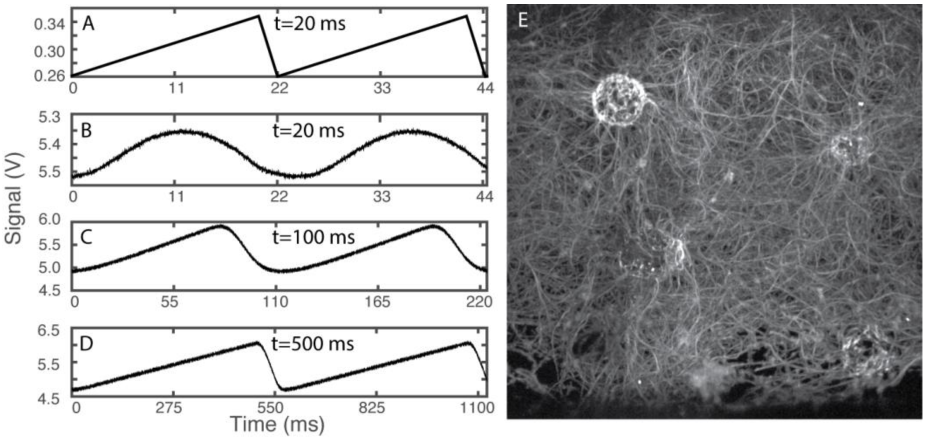

Figure S8. Dynamics of the piezo actuator. (A) Typical waveform used to drive the piezo actuator. (B) Piezo response for a period of 20 milliseconds, (C) 100 milliseconds, and (D) 500 milliseconds. (E) Effect of piezo bandwidth on image formation. XY MIP of fluorescently labeled collagen. Region of decreased intensity (bottom of image) results from loss of synchronization between the piezo and the camera. The image area is 162 x 162 microns.

Supporting Movies

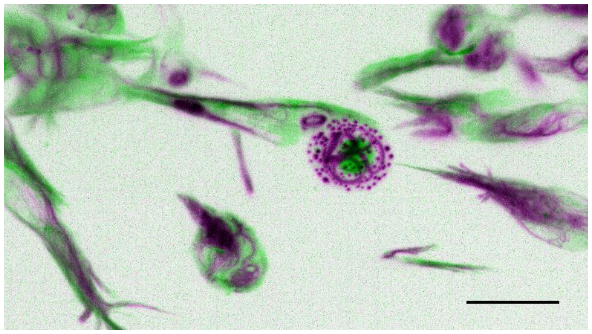

Movie S1. ASLM imaging of collagen-embedded RPE cells labeled with vimentin (magenta) and microtubules (green) over 120 time points. A MIP along the Z-axis over the entire volume is shown. Scale bar 20 microns.

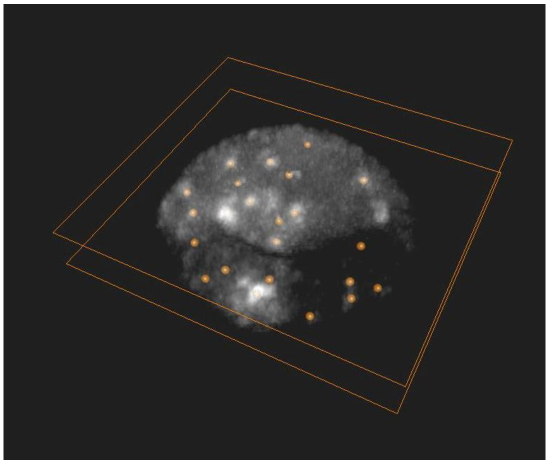

Movie S2. Clathrin coated pit detection in 3D. Local maximum intensity projection with a thickness of 2 microns sweeping through the entire volume of the cell. Detected particles are labeled with spheres.

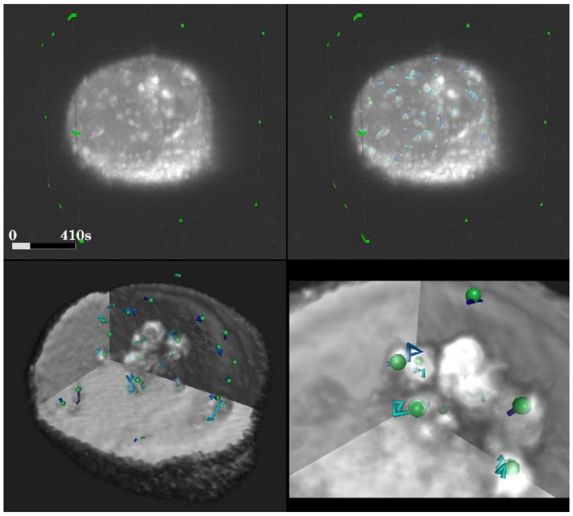

Movie S3. 3D rendering and particle tracking of clathrin-mediated endocytosis in collagen-embedded ARPE cells. (Top Left) 3D maximum intensity projection rendering. Volume encompassing cube is 20 x 20 x 20 microns. (Top Right) Same 3D rendering with particle tracks overlaid. The lifetime of endocytic vesicles is color coded from blue to red, representing shorter to longer lived clathrin coated pits, respectively. (Bottom Left) 3D rendering with ray-casting of the same cell, with a portion of the cell made transparent to facilitate visualization of the clathrin coated pits. (Bottom Right) Detailed view of bottom left panel.

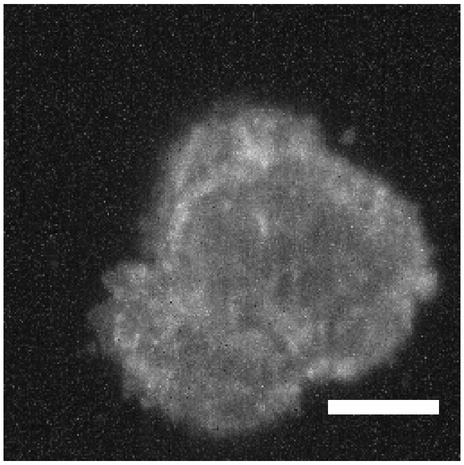

Movie S4. Long time lapse imaging of collagen-embedded RPE-1 cells labeled with Tractin-EGFP spanning 7 hours and 29 minutes and encompassing 600 Z-stacks, acquired in the high-NA mode. Each Z-stack consisted of 251 slices. Cells were continuously imaged with a temporal resolution of 44.9 seconds per Z-stack. Maximum intensity projections along Z provided. A gamma correction of 0.8 was applied to all images to highlight weak features. Scale bar 10 microns.

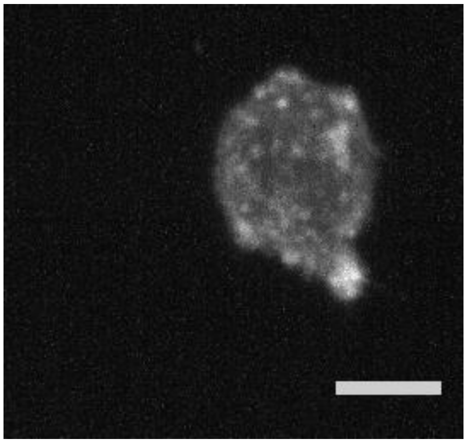

Movie S5. Long time lapse imaging of RPE-1 cells labeled with Tractin-EGFP spanning 10 hours 12 minutes and encompassing 2600 Z-stacks, acquired in the low-NA mode. Each Z-stack consisted of 67 slices. Cells were continuously imaged with a temporal resolution of 13.6 seconds. Maximum intensity projections along Z and only every third slice is shown. A gamma correction of 0.8 was applied to all images to highlight weak features. Scale bar 10 microns.

Supporting References

1. Shaner, N. C., G. G. Lambert, A. Chammas, Y. Ni, P. J. Cranfill, M. A. Baird, B. R. Sell, J. R. Allen, R. N. Day, M. Israelsson, M. W. Davidson, and J. Wang. 2013. A bright monomeric green fluorescent protein derived from Branchiostoma lanceolatum. Nature Methods 10:407-409.
2. Shaner, N. C., M. Z. Lin, M. R. McKeown, P. A. Steinbach, K. L. Hazelwood, M. W. Davidson, and R. Y. Tsien. 2008. Improving the photostability of bright monomeric orange and red fluorescent proteins. Nat Methods 5:545-551.
3. Krahn, K. N., C. V. C. Bouten, S. van Tuijl, M. A. M. J. van Zandvoort, and M. Merkx. 2006. Fluorescently labeled collagen binding proteins allow specific visualization of collagen in tissues and live cell culture. Analytical Biochemistry 350:177-185.
4. Xu, Y., Jorge M. Rivas, Eric L. Brown, X. Liang, and M. Höök. 2004. Virulence Potential of the Staphylococcal Adhesin CNA in Experimental Arthritis Is Determined by Its Affinity for Collagen. The Journal of Infectious Diseases 189:2323-2333.
5. Dean, K. M., and R. Fiolka. 2014. Uniform and scalable light-sheets generated by extended focusing. Optics Express 22:26141.
6. Jaqaman, K., D. Loerke, M. Mettlen, H. Kuwata, S. Grinstein, S. L. Schmid, and G. Danuser. 2008. Robust single-particle tracking in live-cell time-lapse sequences. Nature Methods 5:695-702.
7. Aguet, F., Costin N. Antonescu, M. Mettlen, Sandra L. Schmid, and G. Danuser. 2013. Advances in Analysis of Low Signal-to-Noise Images Link Dynamin and AP2 to the Functions of an Endocytic Checkpoint. Developmental Cell 26:279-291.
8. Gao, L., L. Shao, B.-C. Chen, and E. Betzig. 2014. 3D live fluorescence imaging of cellular dynamics using Bessel beam plane illumination microscopy. Nature Protocols 9:1083-1101.
9. Planchon, T. A., L. Gao, D. E. Milkie, M. W. Davidson, J. A. Galbraith, C. G. Galbraith, and E. Betzig. 2011. Rapid three-dimensional isotropic imaging of living cells using Bessel beam plane illumination. Nature Methods 8:417-423.
10. Chen, B. C., W. R. Legant, K. Wang, L. Shao, D. E. Milkie, M. W. Davidson, C. Janetopoulos, X. S. Wu, J. A. Hammer, Z. Liu, B. P. English, Y. Mimori-Kiyosue, D. P. Romero, A. T. Ritter, J. Lippincott-Schwartz, L. Fritz-Laylin, R. D. Mullins, D. M. Mitchell, J. N. Bembenek, A. C. Reymann, R. Bohme, S. W. Grill, J. T. Wang, G. Seydoux, U. S. Tulu, D. P. Kiehart, and E. Betzig. 2014. Lattice light-sheet microscopy: Imaging molecules to embryos at high spatiotemporal resolution. Science 346:1257998-1257998.